Delft University of Technology

A Novel Technique to Estimate Water Saturation and Capillary Pressure of Foam in Model Fractures

Li, Kai; Wolf, Karl-Heinz A.A.; Rossen, William R.

Citation (APA)
Li, K., Wolf, K.-H. A. A., & Rossen, W. R. (2022). A Novel Technique to Estimate Water Saturation and Capillary Pressure of Foam in Model Fractures. *Colloids and Surfaces A: Physicochemical and Engineering Aspects*, *632*, 1-10. Article 127800. https://doi.org/10.1016/j.colsurfa.2021.127800
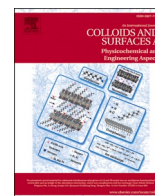
Important note
To cite this publication, please use the final published version (if applicable).
Please check the document version above.

Check for updates

A novel technique to estimate water saturation and capillary pressure of foam in model fractures
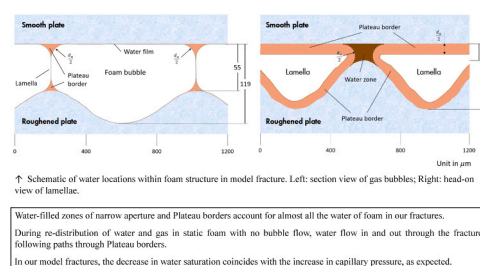
Kai Li [*,1], Karl-Heinz A.A. Wolf, William R. Rossen

Geoscience & Engineering Department, Delft University of Technology, the Netherlands

HIGHLIGHTS

- Glass models with roughened surface are created to represent geological fractures.
- Roughness and aperture distribution of model fractures are characterized.
- Water saturation and capillary pressure of foam in model fractures are estimated.
- Water zones of narrow aperture and Plateau borders account for almost all water in foam.
- Water saturation decreases as capillary pressure increases in model fractures, as expected.

GRAPHICAL ABSTRACT

↑ Schematic of water locations within foam structure in model fracture. Left: section view of gas bubbles; Right: head-on view of lamellae.

Water-filled zones of narrow aperture and Plateau borders account for almost all the water of foam in our fractures.

During re-distribution of water and gas in static foam with no bubble flow, water flow in and out through the fracture following paths through Plateau borders.

In our model fractures, the decrease in water saturation coincides with the increase in capillary pressure, as expected.

ARTICLE INFO

ABSTRACT

Foam is applied in enhanced oil recovery to improve the sweep of injected gas and increase oil recovery, by greatly reducing the mobility of gas. In the laboratory, X-ray computed tomography is commonly used to evaluate the performance of foam in core plugs. However, foam properties, such as bubble size and capillary pressure, are much more difficult to measure. In recent years, microfluidic models have gained much attention because they easily facilitate the imaging study of in-situ foam. However, it is still challenging to estimate capillary pressure, in a model with a uniform depth of etching. In this paper, we report a novel technique to estimate water saturation and capillary pressure of foam in two 1-meter-long model fractures. Both model fractures are made of glass plates. They have different roughness and hydraulic apertures. Unlike microfluidics with uniform depth of etching, our model fractures each has a variation of aperture. We characterize the roughness and represent the aperture distribution of the fracture as a network of pore bodies and pore throats. In this study, foam is pre-generated and then injected into the fractures. The inlet and outlet valves are closed for 24 hr after foam reaches steady-state. We use a high-speed camera to visualize foam in the fractures. We use ImageJ software to analyze foam texture and quantify bubble density, average bubble size and polydispersivity. In addition, we estimate water saturation and capillary pressure by analyzing images in terms of fracture geometry. We found that water in foam resides in locations of narrow aperture, Plateau borders, lamellae between bubbles, and water films on glass walls. Water-filled zones of narrow aperture and Plateau borders account for almost all the water. During the re-distribution of water and gas in static foam, in-flow and out-flow of water must take paths along the network of Plateau borders and water-occupied zones, as they are the only continuous paths for water flow. In both model fractures, the decrease in water saturation coincides with an increase in

* Correspondence to: Department of Geoscience & Engineering, Stevinweg 1, 2628 CN Delft, the Netherlands.
  E-mail address: K.Li-2@tudelft.nl (K. Li).
[1] 0000-0002-9592-2416

capillary pressure, as expected. This novel technique of estimation of water saturation and capillary pressure of foam provides insights for studies of foam in naturally fractured reservoirs with complex geometry, where measuring such foam properties is challenging. This analysis is possible because aperture varies along our model fractures, unlike most microfluidic devices. Our technique would also have an application to foam aquifer remediation and CO_2 sequestration.

Nomenclature

A_{image}	Area of the image
d_a	Local aperture at which water-gas interface locates for a specific water-occupied area fraction
d_{film}	Thickness of water film
d_H	Hydraulic aperture of the model fracture
$d_{lamella}$	Thickness of lamella
$h_{lamella}$	Height of lamella
$L_{lamella}$	Total length of lamellae in the image
L_p	Total length of perimeter of water zones in the image
P_c	Capillary pressure
q_w	Volumetric water injection rate
r_h	Radius of water-gas interfaces viewed from above
S_g'	Gas area fraction
S_w	Water saturation
V_e	Water volume in water along the edge of water zones
V_f'	Defined fracture volume within the region of the images
$V_{lamella}$	Water volume in lamellae
$V_{Plateau\ border}$	Water volume in Plateau borders
V_w	Total water volume
$V_{water\ film}$	Water volume in water films
$V_{water\ zone}$	Water volume in water zones
w	Width of the model fracture
γ_s	Surface tension of the surfactant solution to air at 20 °C
δ_1	Uncertainty of water saturation
δ_2	Uncertainty of capillary pressure
θ	Contact angle
μ_w	Viscosity of water
∇P_w	Pressure gradient of water flow

---

1. Introduction

Foam is a dispersion of gas in liquid, where gas bubbles are separated by interconnected aqueous films. The films, called lamellae, are stabilized by surfactants [1,2]. Foam has many applications in underground settings. In acid stimulation, foam can be used as a diverting agent in almost every type of completion to improve stimulation coverage across the zone of interest [3]. In aquifer remediation [4], foam is applied to selectively block high-permeability layers, and displace dense non-aqueous phase liquid (DNAPL) from low-permeability layers that are often unswept during a conventional remediation process. In enhanced oil recovery (EOR), foam can effectively mitigate all conformance problems by reducing the mobility of gas by a factor of hundreds or more [5].

Foam in EOR has been studied theoretically and experimentally for decades [6-8]. During foam injection, gas relative permeability is reduced due to gas trapping, and gas apparent viscosity is increased due to capillary forces and drag on moving lamellae. The mobility of gas is thus greatly reduced. As a result, the displacement front is more stable, and more gas is diverted to unswept zones, hence improving sweep, reducing gas/oil ratio, and increasing oil recovery [9,10].

Foam is a non-Newtonian fluid and exhibits low- and high-quality flow regimes [11-13]. In foam, foam quality is defined as the ratio of gas volumetric flow rate to the total rate. In the low-quality regime, the apparent viscosity of foam is controlled by gas superficial velocity and it increases as foam quality increases. Foam displays shear-thinning rheology in this regime. In the high-quality regime above the critical foam quality, the limiting capillary pressure is reached and foam becomes unstable. Apparent viscosity in this regime is controlled by liquid superficial velocity and it decreases as foam quality increases.

Foam pilots have also been implemented in naturally fractured reservoirs (NFRs) in the past three decades. By building up a viscous pressure gradient in fractures, foam can divert the flow of gas into the matrix, hence delaying gas breakthrough, reducing gas/oil ratio, and improving oil production [14-16]. Friedmann et al. [17] reported a foam pilot in the Rangely field that was characterized as a sand unit with hydraulic fractures, natural fracture networks, reservoir heterogeneity,

and injection/production imbalance. They found that the gelled foam improved volumetric sweep, reduced CO_2 recycling, and increased oil production at a lower cost than traditional polymer gel. Ocampo-Florez et al. [18] presented two successful foam EOR field pilots in the naturally fractured Cupiagua in Recetor field. They used the technique of gas tracer to study foam and confirmed gas diversion deep in the reservoir and improvement in sweep efficiency. They found that foam mitigated gas recycling and increased oil/condensate recovery. In the tight, fractured reservoir in Woodbine, Katiyar et al. [19] reported an immiscible hydrocarbon foam pilot. The injection strategy of surfactant alternating gas (SAG) was adopted. They observed an increased oil production rate and an increased gas utilization ratio. Foam was also successfully implemented in the naturally fractured gas-condensate Piedemonte field [20]. By dispersing surfactant solution in the hydrocarbon gas, a delayed gas breakthrough and a reduction of gas/oil ratio were achieved. However, bubble texture of foam and foam properties such as water saturation and capillary pressure haven't been examined in these studies.

In geological porous media, foam with a finer texture (smaller bubbles) and larger bubble density gives a greater reduction of gas mobility, hence an improved sweep and oil recovery [21]. In the laboratory, X-ray computed tomography (CT) is commonly used to evaluate the performance of foam in core plugs [22,23]. A greater pressure gradient indicates finer-texture foam with greater gas mobility control. Water saturation is mapped at different times of the foam process to study foam behavior. X-ray CT is capable of showing the displacement profile of foam injection. However, bubble size and capillary pressure are much more difficult to measure.

In recent years, a microfluidic device, a network of channels and pillars with uniform depth and widths of tens to hundreds of microns, is increasingly useful for foam study. It provides possibilities to replicate the complex geometry of 2D porous media, and its transparency allows direct observation of foam at the pore scale. Gauteplass et al. [24] carried out foam experiments in an etched-silicon micromodel. By studying lamella movement in the interior of the pore bodies and at permeability discontinuities, they identified snap-off as the main mechanism for in-situ foam generation. AlQuaimi and Rossen [25] studied foam in a variety of glass model fractures (length × width: 400 × 100 mm) with

different geometry and variable aperture. By using a microscope, they investigated foam generation and propagation in the fractures. They also quantified bubble density and bubble size in the foam, and explained the effects of fracture geometry on these foam properties. Jones et al. [26] studied gas trapping in a microfluidic model and reported a strong response of trapped-gas fraction to velocity variations. The fraction of trapped gas increased from 12% to 63% as superficial velocity dropped from 400 to 50 mm/s. They argued that at lower velocities bubbles had a higher probability to coarsen to pore size, and in the process, more effectively blocking individual pores and increasing the trapped-gas fraction. Microfluidic models facilitate direct visualization of foam and quantification of bubble texture. However, it is still challenging to estimate capillary pressure, because they have a uniform depth of etching.

In this study, we have built two 1-meter-long model fractures with different roughness and hydraulic apertures to study foam texture and estimate water saturation and capillary pressure. Unlike microfluidics with uniform depth of etching, our model fractures have a variation of aperture. In this paper, we first present the experimental setup and materials. We then study the roughness and characterize the aperture distribution of the fractures. We then describe the experimental method and approach to image analysis. Lastly, we explain how we estimate water volume in the fractures and present results of water saturation and capillary pressure of foam in our model fractures.

2. Experimental setup and materials

Fig. 1 shows the experimental setup. We use a mass-flow controller (Bronkhorst Nederland B.V., F-230 M, range: 0.19–10 mL/min) to inject gas, and a dual-cylinder pump (VINDUM Engineering, INC., Model VP1–12 K, range: 0–28 mL/min) to inject liquid. A mixing tee with a frit inside (Upchurch Scientific, PEEK™, UHMWPE frit, mesh size: 10 μm) is installed upstream of the inlet of the fracture to pre-generate foam. Two absolute pressure transducers (DEMO MPXH6400A, range: 4 bar, accuracy: ± 10 mbar) are mounted on the fracture to measure pressure at the inlet and the outlet.

In our study, we create two model fractures, Model 1 and Model 2, with the same dimension of $1 \times 0.15 \times 0.04$ m (length- $\times$ width $\times$ thickness). Each model is made of two 2 cm-thick glass plates (Hijman Glas B.V., the Netherlands). The top glass plate is smooth and the bottom plate is roughened on the side facing the top plate. The roughness of the bottom roughened plate is created by moulding during the manufacturing process. The glass plates are strongly water-wet and the contact angle θ is close to 0 °. To create a model, we place the two plates directly against each other and glue them along edges using SR1–40B Silicon rubber. The model is then housed in an aluminum clamping frame (Fig. 2). The gap between the two plates represents a

geological fracture aperture. We drill six holes through the roughened plate for foam injection and discharge, and for linking to the pressure transducers. Two troughs (length $\times$ width $\times$ depth: $12 \times 2 \times 0.04$ cm) are milled in the rough plate. The one at the inlet facilitates an even foam injection into the fracture along its width. The one at the end of the fracture prevents converging foam flow at the outlet.

We use a high-speed high-resolution micro-camera (Photron Fastcam UX50, up to 160,000 fps) to visualize and record images of foam inside the model fractures. A back-light source (VAL LED lighting, VL-CB-CL), mounted under the fracture, provides high-parallelism light for the camera. The whole setup is placed inside a black tent to improve the imaging quality.

In this study, we inject a solution of 1 wt% AOS C14–16 surfactant (Stepan® BIO-TERGE AS-40 KSB, Active content: 39%, molecular weight: 324 g/mol) and nitrogen (Linde Gas Benelux B.V., Purity $\geq$ 99.999%) to create foam. The surface tension γ_s of the surfactant solution to air at 20 °C is 32.2 mN/m, measured using a KSV Sigma Tensiometer.

3. Roughness and aperture distribution of model fractures

In our study, Model 1 and Model 2 have different roughness. Model 1 has the roughness in a regular pattern, while Model 2 has the roughness in an irregular pattern. Fig. 3 shows relative height of the different roughened plates of the two models. With a smooth plate on top, each model fracture provides a slit-like channel with variation in aperture for foam flow. We measure hydraulic aperture d_H of the fractures prior to foam experiments, by injecting demineralized water (ELGA VEOLIA Labwater) through the pre-vacuumed fractures at stepwise-increasing volumetric rates q_w. The pressure gradient of steady-state water flow, ∇P_w, is recorded at each injection rate. A regression of pressure gradient against the injection rate determines d_H [27]:

$$|\nabla P_w| = 12 \quad q_w \frac{1}{w} \frac{1}{d_H^3} \quad \mu_w \tag{1}$$

where w is the width of the model fracture, and μ_w is water viscosity. The hydraulic aperture of Model 1 and Model 2 obtained from Eq. 1 are 46 and 78 μm, respectively.

In addition, we measure fracture volume of the two models by injecting demineralized water into the models (after first vacuuming) while closing the outlet valve. We stop the injection once the models are fully saturated with water. The volume of water injected by the pump is estimated to be the fracture volume. In our study, the fracture volume of Model 1 and Model 2 are 9.1 and 14.2 mL, respectively. Using the value of fracture volume and relative height data of the roughened plate, we
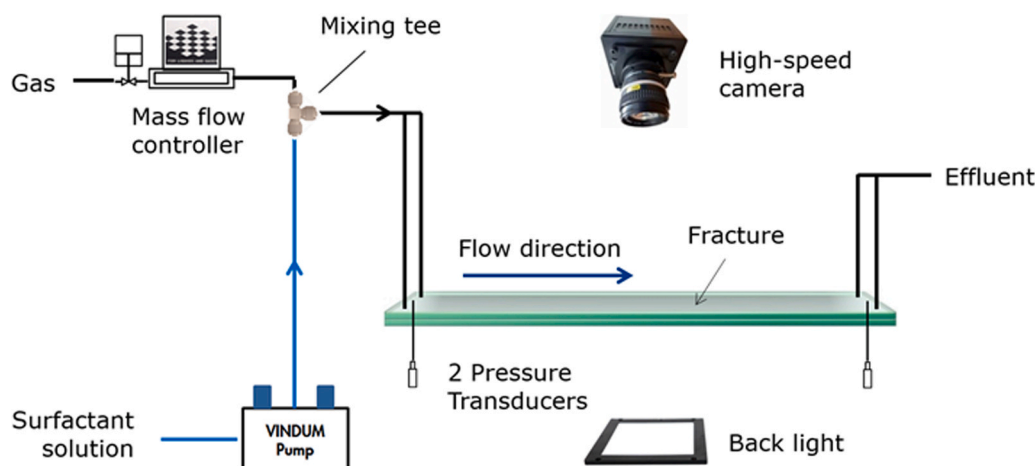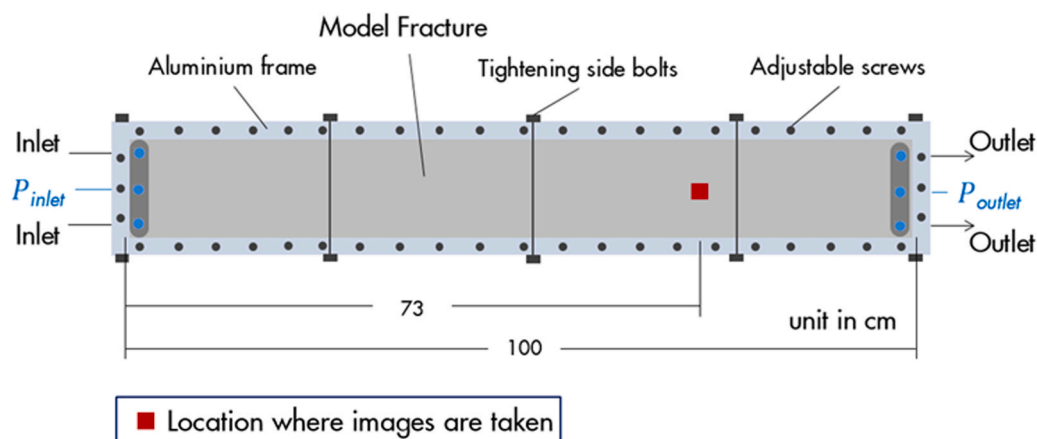

Fig. 1. Experimental setup.

Fig. 2. Model fracture in the aluminum clamping frame. The red square indicates the location where images of foam shown in this study are taken.
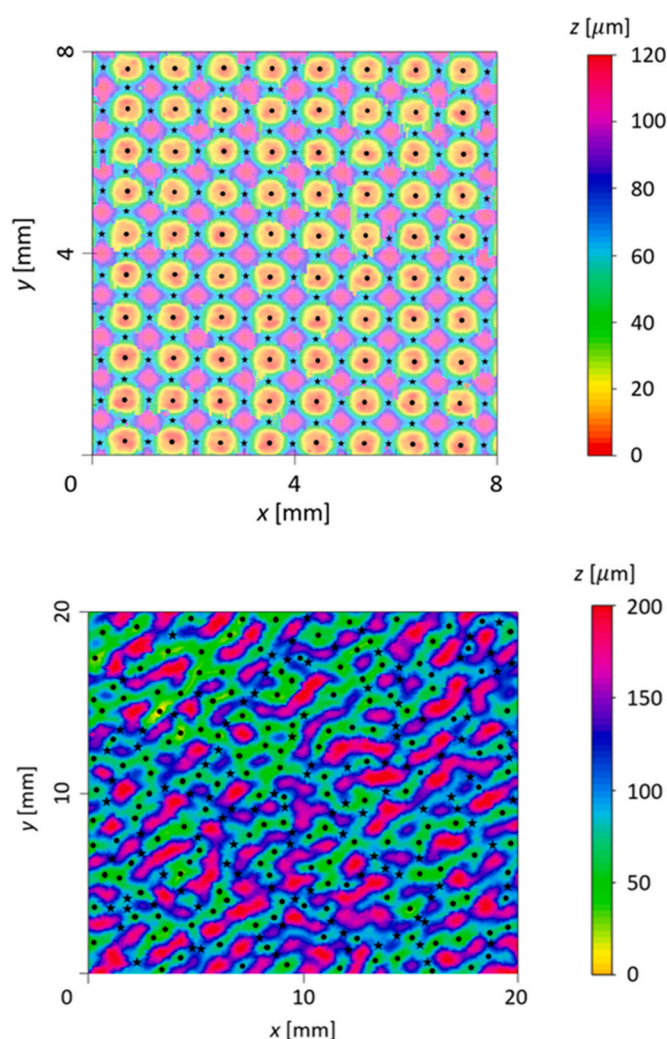

Fig. 3. Top: relative height of the roughened plate of Model 1 (regular pattern); resolution: 960×960, pixel size: $69 \ \mu m^2$; Bottom: relative height of the roughened plate of Model 2 (irregular pattern); resolution: 2860×2860, pixel size: $49 \ \mu m^2$. Black stars are saddle points on the roughened plate, and black dots are local minima in height. The height data are profiled using a digital microscope (Keyence, VHX-7000).

calculate aperture distribution of each model.

With local hills (maxima of height) and valleys (minima of height) on the roughened plates, the distribution of aperture of both models can be represented as a 2D network of pore bodies and pore throats. Thus, with pore bodies and throats, the model fractures are similar in some ways to microfluidic porous media. As shown in Fig. 3, we define pore bodies at local minima of height on the roughened plate, and pore throats, which connect pore bodies, at saddle points between pore bodies. We measure the heights of these local minima and saddle points and convert them to apertures using aperture distribution. We then average apertures at local minima to estimate typical aperture of pore bodies and average apertures at saddle points to estimate typical aperture of pore throats. In Model 1, each pore body has one local minimum of height and is connected to other four pore bodies through pore throats. In Model 2, there may be multiple local minima (with only slightly different height) for each pore body on the roughened plate. We consider these to represent one pore body. Table 1 shows the properties of our two model fractures.

4. Foam experiments and image analysis

Prior to foam injection, the model fracture is thoroughly cleaned by flooding 20 fracture pore volume of demineralized water, then vacuumed and pre-saturated with surfactant solution. We pre-generate foam by injecting surfactant solution and gas through the mixing tee (mesh size of inside-mounted frit: 10 μm) at foam quality (ratio of gas volumetric injection rate to total rate) of 0.9, and at total interstitial velocity of 1.2 and 2 mm/s for Model 1 and Model 2, respectively. Foam is then injected into the horizontally-placed fracture. The pre-generation, combined with considerable foam coarsening by diffusion between the mixing tee and the entrance of the fracture, ensures that gas enters the fracture as relatively large bubbles instead of gas slugs. Within the model fracture, foam is further refined during propagation due to in-situ bubble generation. After foam flow reaches steady-state, bubble generation and destruction rates are in local equilibrium in the second half of the model fracture [28]. We close inlet and outlet valves, and set

Table 1
Properties of Model 1 and Model 2.

	Hydraulic aperture, μm	Fracture volume, mL	Typical pore throat aperture, μm	Typical pore body aperture, μm
Model 1 (regular roughness)	46	9.1	55	119
Model 2 (irregular roughness)	78	14.2	92	174

time to zero at this point for our experiments. The model fracture is then shut in for 24 hr at 20 °C.

After shut-in, water and gas flow along the model fractures to equalize pressure. At the beginning of the shut-in period, foam continues to flow governed by residual pressure gradient. Once pressure gradient dissipates (at time 0.08 hr for Model 1, and 0.1 hr for Model 2), foam mostly stops flowing and starts to coarsen due to diffusion between bubbles. As a result, some bubbles disappear as all their gas diffuses into neighbouring bubbles, and the remaining bubbles enlarge in size. During coarsening, trains of bubbles occasionally flow along separate pathways from outlet toward inlet. This evidently results from a pressure gradient from outlet toward inlet due to a small leak in the tubing upstream of the models. We also observed rare coalescence (rupture of lamellae) along the convections. However, the convection of bubbles along separate pathways and coalescence of lamellae have small effects on average bubble size and haven't significantly affected the overall behavior of foam coarsening in our study. Moreover, water is transported along our models even during periods with no bubble flow.

To study these behaviors, and estimate water saturation and capillary pressure of foam, we take images of foam at different times. The figures shown here are taken at a location 73 cm from fracture inlet (Fig. 2) where foam reaches local equilibrium at time zero. We use ImageJ software to process raw foam images. Fig. 4 shows raw and processed images of foam in Model 1 at 0.08 hr and Model 2 at 0.1 hr. We distinguish gas and water phase in the foam by tuning the threshold of the grey values of pixels. Gas bubbles and lamellae are thus identified in binarized foam images. We can quantify foam texture by measuring bubble density (number of bubbles per unit area of image), 2D average bubble size and polydispersivity, and gas area fraction S_g'. Unlike microfluidics with uniform depth of etching, our model fractures have a variation of aperture with the presence of hills and valleys on the roughened plates (Fig. 3). As a result, there are local accumulations of water (water zones) in locations with tighter aperture within the model fractures, as governed by capillarity. We distinguish these water zones and lamellae to calculate water-occupied area fraction as illustrated in

Fig. 4, and then skeletonize all lamellae in the image to sum up their lengths.

In addition, we correlate the histogram of height on the roughened plate and water-occupied area fraction to estimate the aperture d_a, where water-gas interfaces locate at the edge of the water-occupied areas. In foam, the Plateau borders form an interconnected network for water to redistribute and capillary pressure to equalize. We assume that one interface would have the same aperture d_a as others within the area of our images due to uniform capillary pressure in that area of the fracture. Fig. 5 shows the histogram of height and its cumulative area fraction. Using the value of aperture d_a, we estimate capillary pressure, and from that the radius of Plateau borders and the height of lamellae between the Plateau borders.

5. Water saturation and capillary pressure of foam

In this study, we assume that contact angle θ is 0, as water strongly wets both glass model fractures. Fig. 6 shows a schematic of foam in Model 1. The gap between the plates is much less than the radius of curvature of the water-gas interface as viewed from above (see images of lamellae in Fig. 4). All water-gas interfaces are thus close to cylindrical. In our model fractures, water exists in four locations: water zones, Plateau borders, lamellae, and water films that wet fracture walls above and below.

As shown in Fig. 4, water zones accumulate in locations with tighter aperture in our model fractures. We thus use histogram of height data on the roughened plates (Fig. 5) to correlate water-occupied area fraction and volume of water zones, $V_{water\ zone}$. Fig. 7 shows the correlation for the two model fractures. The calculation of water volume in different locations in our model fractures in this paper is based on a defined fracture volume V_f' within the region of the images shown in Fig. 4: 1.03 and 11.44 mm^3 within a region of 52.9 and 120.8 mm^2 for Model 1 and Model 2, respectively.

In our model fractures, we observe only foam with bubbles extending from top to bottom plates. Plateau borders form where lamellae meet
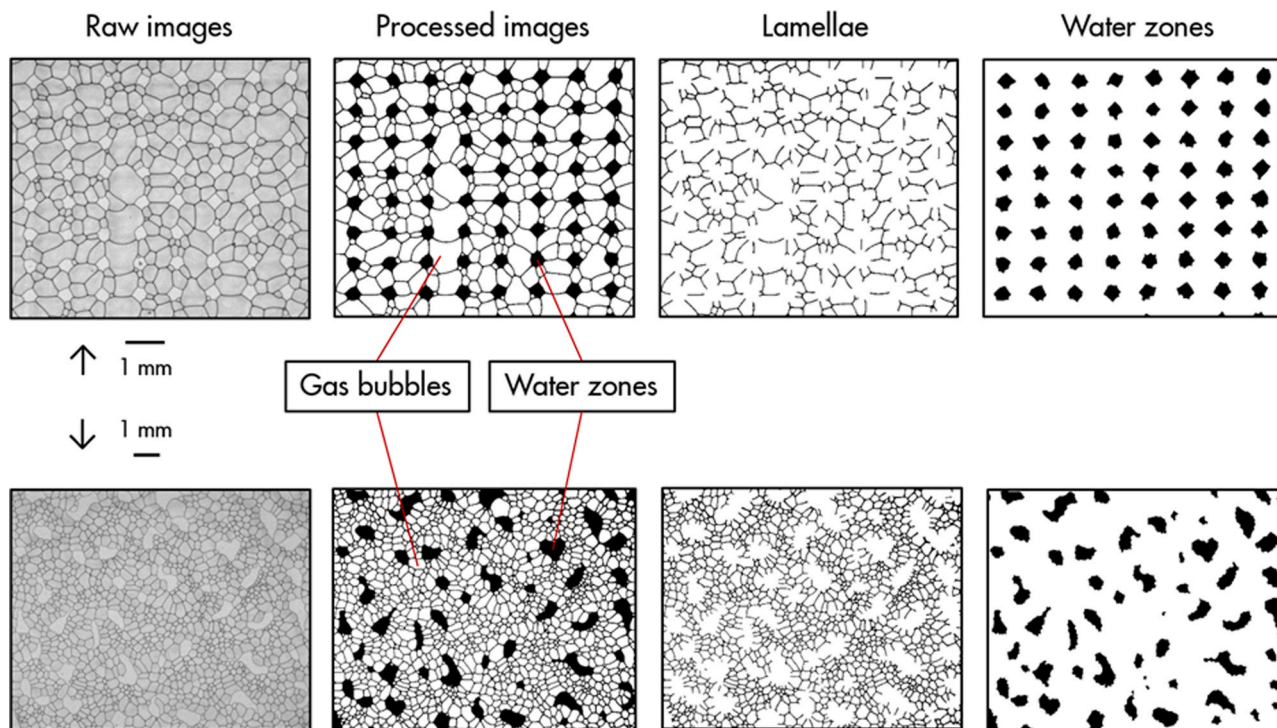

Fig. 4. Raw and processed images of foam. Top: in Model 1 at 0.08 hr, image size: 7.8 × 6.8 mm; Bottom: in Model 2 at 0.1 hr, image size: 12.3 × 9.8 mm. Water is shown in black, gas in white. Water zones occupy locations with tighter aperture in the model fractures.
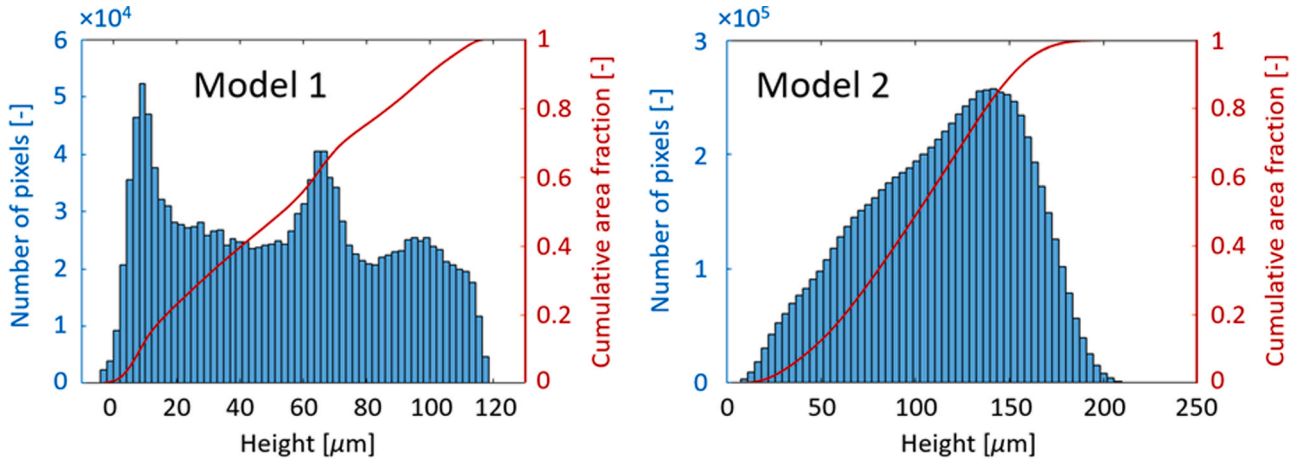
Fig. 5. Histogram of height of the roughened plate and cumulative area fraction of Model 1 (Left) and Model 2 (Right).
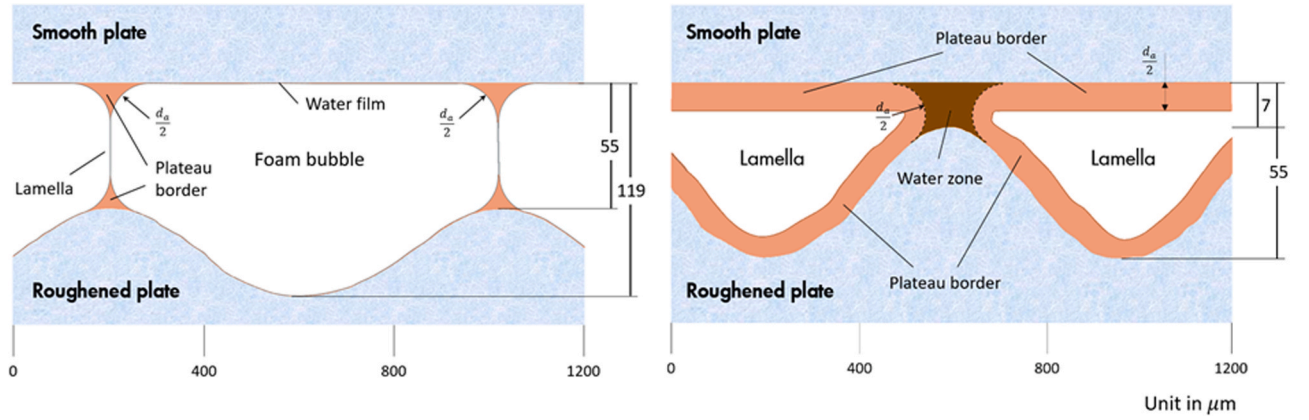

Fig. 6. Schematic of foam texture in Model 1 for a case where bubbles each fill the pore body. Left: section view of gas bubbles in pore bodies, with lamellae in pore throats; Right: head-on view of lamellae located at pore throats and water zone located at the location with tighter aperture. d_a is the local aperture of water-gas interfaces. Vertical scale is greatly exaggerated.
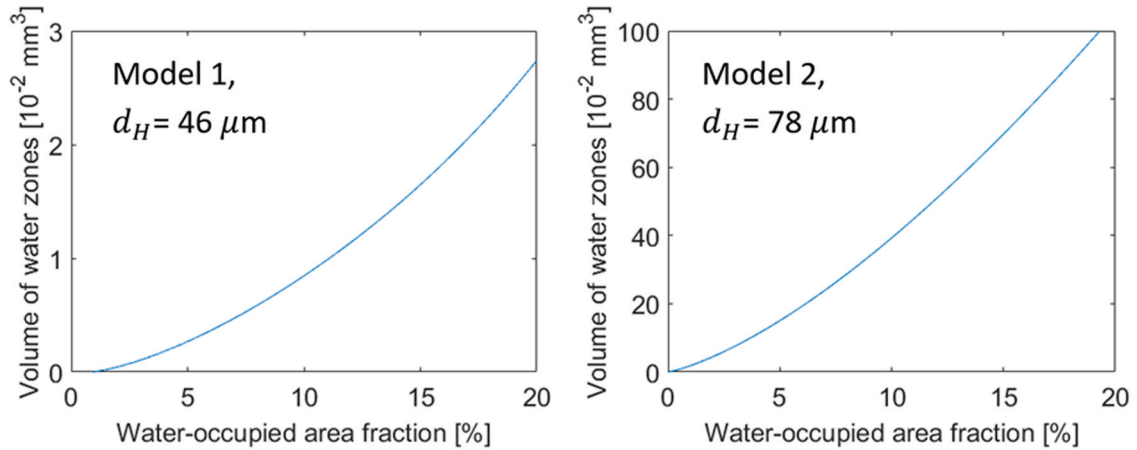

Fig. 7. Correlation of water-occupied area fraction and volume of water zones for Model 1 (Left) and Model 2 (Right). Volume of water zones is based on a defined fracture volume of 1.03 and 11.44 mm³ for Model 1 and Model 2, respectively.

glass plates above and below. Under strongly water-wet conditions, as here, the radius of the Plateau borders is half of the local aperture of water-gas interfaces d_a. The volume of water in Plateau borders is then given by:

$$V_{Plateau\ border} = (\frac{4 - \pi}{4})d_a^2 L_{lamella} \tag{2}$$

where $L_{lamella}$ is the sum of lengths of all lamellae in the image.

A small amount of water exists in sub-microscopic lamellae and

water films along the glass plates. We estimate the volume of water in lamellae and water films by:

$$V_{lamella} = L_{lamella} \cdot d_{lamella} \cdot h_{lamella} \tag{3}$$

$$V_{water\ film} = 2S_g' A_{image} d_{film} \tag{4}$$

where $d_{lamella}$ and $h_{lamella}$ are the thickness and height of lamella, d_{film} is the thickness of water film, S_g' is the gas area fraction, and A_{image} is the area of the image. Both $d_{lamella}$ and d_{film} depend on the surfactant, salinity and capillary pressure. In this study, we assume both to be 30 nm [29, 30]. As shown in Fig. 6 Left, lamellae connect Plateau borders on the smooth plate above and the roughened plate below. We approximate $h_{lamella}$ as $d_H - d_a$, where d_H is the hydraulic aperture of the model fracture, and d_a is the local aperture of water-gas interfaces.

We have observed that there are no local water-occupied zones (water zones) at positions of narrow apertures in Model 1 after 5 hr. It is then difficult to estimate the local aperture of water-gas interfaces, and from that the radius of Plateau borders, water saturation and capillary pressure. It is nevertheless evident that the out-flow water rate is greater than the in-flow water rate at location 73 cm from the inlet of Model 1. The water saturation after 5 hr there is at least lower than that at 1.7 hr, with greater capillary pressure.

Fig. 8 shows water volume in different locations. Water zones and Plateau borders account for almost all water in foam. In both models, as water in the Plateau borders decreases, the reduction of sum-up water volume also slows down with time. This is because, during the period of shut-in, if bubbles do not move, the in-flow and out-flow of water must take the paths through Plateau borders and water zones.

We calculate water volume V_w and water saturation S_w by:

$$V_w = V_{water\ zone} + V_{Plateau\ border} + V_{lamella} + V_{water\ film} \tag{5}$$

$$S_w = \frac{V_w}{V_f'} \tag{6}$$

where V_f' is the fracture volume within the region of the images shown in Fig. 4 (1.03 and 11.44 mm^3 for Model 1 and Model 2, respectively).

We estimate capillary pressure of foam P_c at a specific time by:

$$P_c = \frac{2\gamma_s cos\theta}{d_a} \tag{7}$$

where γ_s is the surface tension of the surfactant solution, θ is the contact angle, and d_a is the local aperture of water-gas interfaces. In this study, we assume that contact angle θ is 0, as water strongly wets the glass model fractures.

Fig. 9 shows the results of S_w and P_c at different times during the

experiments in the two models. In both model fractures, the decrease in water saturation coincides with the increase in capillary pressure, as expected. The decrease in water saturation is due to the small leak upstream of the fracture inlet and consequent upstream flow of water. Compared to Model 2, foam in Model 1 evolves under higher capillary pressure.

In this paper, we have studied aperture distribution of two model fractures with different roughness. By analyzing foam images, we directly studied foam texture and estimated water saturation and capillary pressure in the fractures. Table 2 presents the results of water volume in different locations, water saturation and capillary pressure of foam in the two model fractures.

The estimation of capillary pressure, crucial to our approach, is made possible by the variation of aperture with position in the models. This approach would not work in microfluidic devices with uniform depth of etching. The interconnected network of Plateau borders in foam is also essential to our assumption that water can redistribute, in a foam where bubbles are immobile, to equalize capillary pressure within the region of the images.

6. Estimated uncertainty of water saturation and capillary pressure

In this paper, calculated water volume comprises four locations in the model fractures. To this end, we convert water-occupied area fraction to water volume in water zones (as one of the four locations) using an integral-based correlation (Fig. 7). In raw images of foam (Fig. 4), water-gas interfaces around water zones appear as lighter boundaries compared to darker Plateau borders, which also mark the location of lamellae. Using ImageJ software, we identified water zones to compute water-occupied area fraction (Fig. 4). We further correlated height histogram of the roughened plate and water-occupied area fraction to estimate the local aperture d_a at water-gas interfaces, by which we estimated capillary pressure of foam (Eq. 7).

As shown in Fig. 10, in our imaging, we assume that the edge boundaries of water zones shown in processed foam images are in positions of the leading edges of the curved water-gas interfaces, as the refractive index of water is closer to that of glass compared to gas. Therefore, there is a part of water along the edge of water zones, which is not included in previous calculation of water volume. The uncertainty of water saturation δ_1 due to this is given by:

$$\delta_1 = \frac{V_e}{V_f'} = \left(\frac{4-\pi}{8}\right)\frac{d_a^2\ L_p}{V_f'} \tag{8}$$

where V_e is the volume of the water along the edge of water zones in the images (shown in purple in the schematic of Fig. 10), V_f' is the fracture
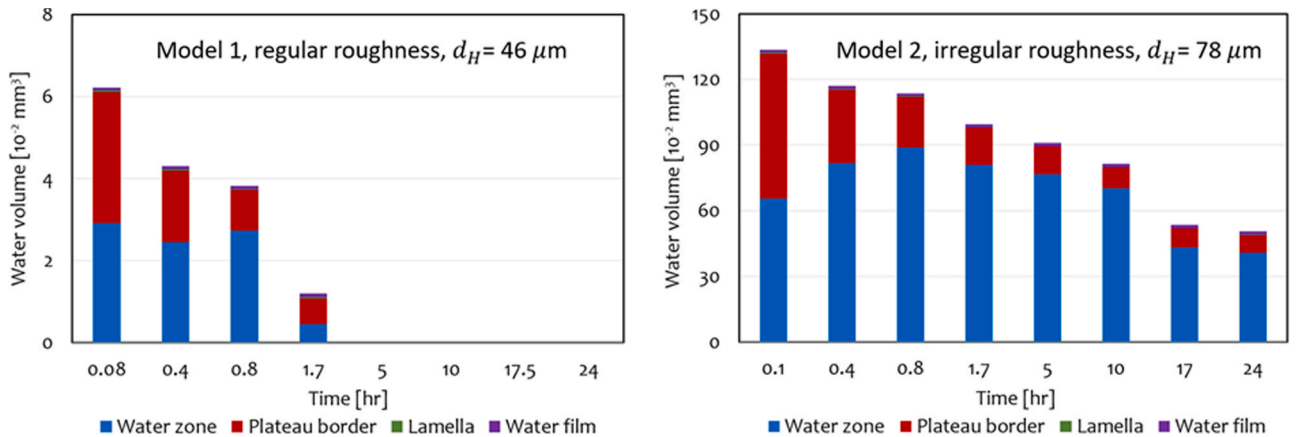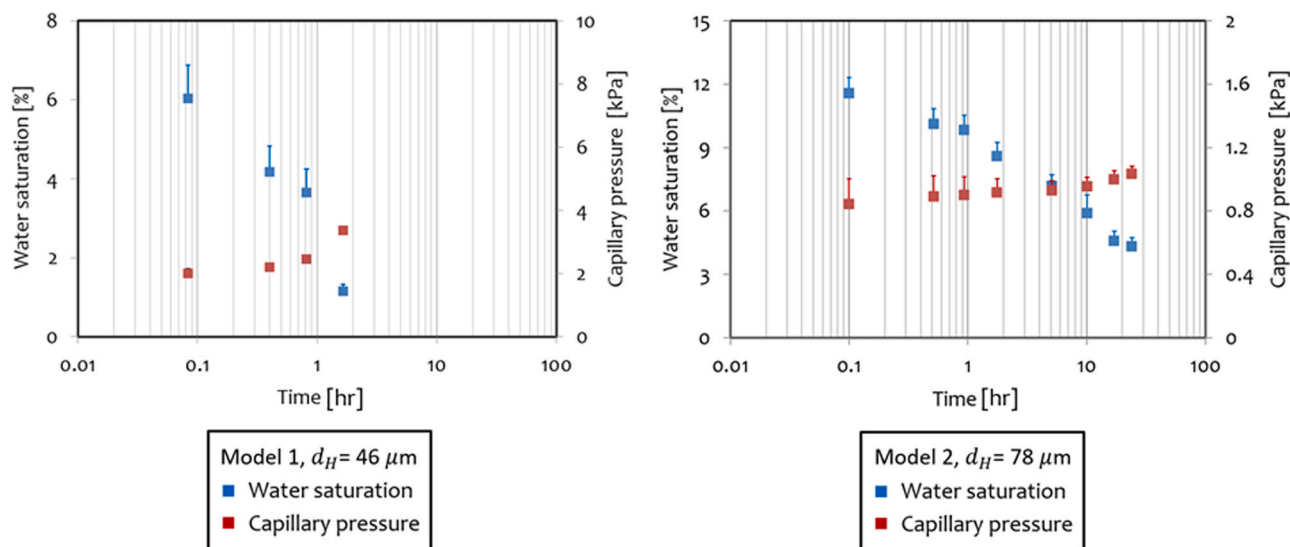

Fig. 8. Water volume in water zones, Plateau borders, lamellae and water films in Model 1 (Left) and Model 2 (Right).

Fig. 9. Water saturation and capillary pressure of foam in Model 1 (Left) and Model 2 (Right). The positive error bar on the data reflects the uncertainty of water saturation and capillary pressure estimation. The calculation of the uncertainty is described in the next Section.

Table 2
Results of water volume in different locations, water saturation and capillary pressure in the two model fractures. The calculation of water volume in different locations is based on fracture volume V_f' within the image region: 1.03 and 11.44 mm^3 for Model 1 and Model 2, respectively. Data in Model 1 after 5 hr are not presented, because there are no water zones at locations of narrow apertures and it is then difficult to estimate the local aperture of water-gas interfaces for these calculations.

	Time, hr	Aperture at water-gas interfaces, d_a, μm	Water volume in water zones, $V_{water\ zone}$, 10^{-2} mm^3	Water volume in Plateau borders, $V_{Plateau\ border}$, 10^{-2} mm^3	Water volume in lamellae, $V_{lamella}$, 10^{-2} mm^3	Water volume in water films, $V_{water\ film}$, 10^{-2} mm^3	Total water volume, V_w, 10^{-2} mm^3	Water saturation, S_w, %	Capillary pressure, P_c, kPa
Model 1 (regular roughness), $d_H = 46$ μm	0.08	32	2.92	3.18	0.04	0.08	6.23	6.0	2.01
	0.4	29	2.45	1.73	0.03	0.09	4.30	4.2	2.21
	0.8	26	2.74	0.98	0.02	0.09	3.83	3.7	2.46
	1.7	19	0.45	0.63	0.02	0.10	1.20	1.2	3.37
	5								
	10								
	17.5								
	24								
Model 2 (irregular roughness), $d_H = 78$ μm	0.1	76	65.53	66.15	0.53	1.30	133.52	11.6	0.84
	0.4	72	81.66	33.55	0.30	1.40	116.91	10.1	0.89
	0.8	71	88.75	23.24	0.21	1.43	113.64	9.8	0.90
	1.7	70	80.74	17.01	0.16	1.48	99.39	8.6	0.91
	5	69	71.73	9.69	0.12	1.58	83.13	7.2	0.93
	10	67	61.11	9.21	0.10	1.56	71.98	5.9	0.96
	17	64	43.12	8.74	0.10	1.61	53.57	4.6	1.00
	24	62	40.60	8.19	0.10	1.64	50.53	4.3	1.03

volume within the image region, d_a is the local aperture of water-gas interfaces, and L_p is the total length of perimeter of water zones in the images.

In addition, capillary pressure calculated using Eq. 7 assumes that water-gas interfaces are cylindrical with only one principle direction of curvature, because aperture of the interfaces (tens of microns) is much smaller than the radius of the interfaces r_h viewed from above (hundreds of microns). Thus, the estimation uncertainty of capillary pressure δ_2 by ignoring principal radius r_h is given by:

$$\delta_2 = \frac{\gamma_s}{r_h}\ cos\theta \qquad (9)$$

Using Eqs. 8 and 9, we obtain the uncertainty of our methods in estimating water saturation and capillary pressure. We present these values in Table 3.

7. Conclusions

In this study, we built two 1 m-long glass model fractures, similar in

some ways to microfluidic porous media, to study foam behavior in naturally fractured reservoirs. Using ImageJ software, we report a novel technique to analyze foam texture, and especially to estimate water saturation and capillary pressure of foam. We show that, in fractures, water in foam lies in four locations: water zones, Plateau borders, lamellae, and water films on glass plates. We analyze the roughness and characterize the geometry of fractures. We correlate the histogram of height on the roughened plates and water-occupied area fraction to estimate the local aperture of water-gas interfaces. Using imaging analysis, we calculate water volume in the four different locations, and estimate water saturation and capillary pressure. We conclude that water zones and Plateau borders account for almost all the water of foam in fractures. During re-distribution of water and gas in static foam after shut-in, water flow in and out through the fracture following paths through Plateau borders and water zones, which are the only continuous paths for water flow. In both model fractures, the decrease in water saturation coincides with the increase in capillary pressure, as expected. The uncertainty analysis in Section 6 confirms that our technique is reasonably accurate. Foam texture and properties including water saturation and capillary
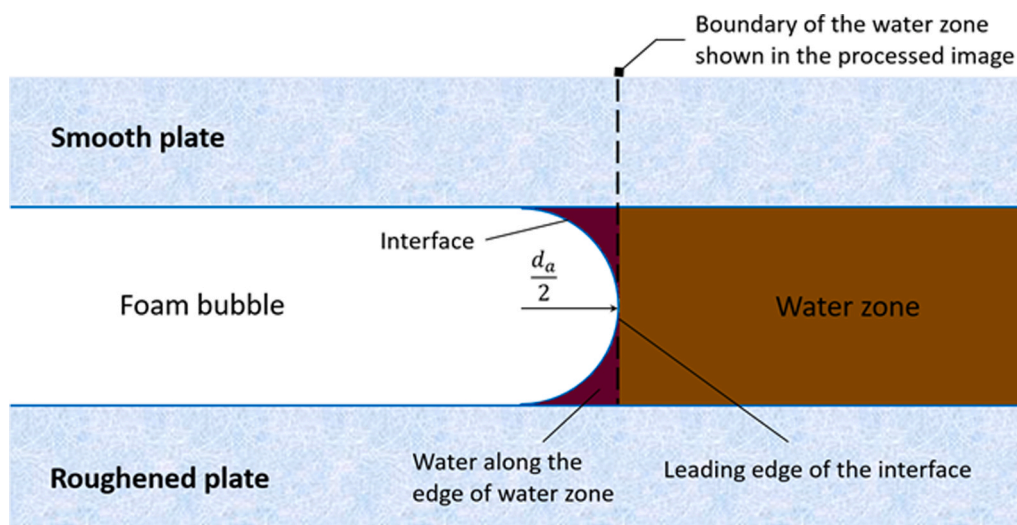
Fig. 10. Schematic of a foam bubble contacting a water zone in the fracture. The dashed line marks the boundary location of the water zone shown in the processed foam image.

Table 3
Uncertainty of water saturation and capillary pressure of foam in two model fractures. The calculation of water volume along the edge of water zones is based on fracture volume V_f' within the image region: 1.03 and 11.44 mm^3 for Model 1 and Model 2, respectively. Data in Model 1 after 5 hr are not presented, because there are no water zones at locations of narrow apertures and it is then difficult to estimate the local aperture of water-gas interfaces for these calculations.

	Time, hr	Water saturation, S_w, %	Capillary pressure, P_c, kPa	Total length of perimeter of water zones, L_p, mm	Volume of water along the edge of water zone, V_e, 10^{-2} mm^3	Principle radius of interfaces in parallel with the fracture plane, r_h, μm	Uncertainty of water saturation, δ_1, %	Uncertainty of capillary pressure, δ_2, kPa
Model 1 (regular roughness), d_H = 46 μm	0.08	6.0	2.01	79	0.87	200	0.8	0.15
	0.4	4.2	2.21	75	0.68	281	0.7	0.11
	0.8	3.7	2.46	76	0.55	355	0.6	0.09
	1.7	1.2	3.37	44	0.17	429	0.2	0.07
	5							
	10							
	17.5							
	24							
Model 2 (irregular roughness), d_H = 78 μm	0.1	11.6	0.84	118	7.34	198	0.8	0.16
	0.4	10.1	0.89	128	7.15	240	0.7	0.13
	0.8	9.8	0.90	127	6.85	282	0.7	0.11
	1.7	8.6	0.91	122	6.41	358	0.7	0.09
	5	7.2	0.93	102	5.19	498	0.6	0.06
	10	5.9	0.96	111	5.33	563	0.9	0.06
	17	4.6	1.00	95	4.18	606	0.5	0.05
	24	4.3	1.03	89	3.68	615	0.4	0.05

pressure have often been left unmeasured in previous studies. Our technique provides useful insights for studies of foam in porous media with complex geometry, where measuring such foam properties is challenging. This analysis is possible because our model fractures have variable aperture, unlike most microfluidic devices with uniform depth of etching. Our technique would also have an application to foam aquifer remediation and CO$_2$ sequestration.

CRediT authorship contribution statement

William R. Rossen: Conceptualization, Methodology, Data analysis, Supervision, Writing – review & editing. Kai Li: Conceptualization, Methodology, Software, Data analysis, Writing – original draft, Writing – review & editing. Karl-Heinz Wolf: Methodology, Supervision, Writing – review & editing.

Declaration of Competing Interest

The authors declare that they have no known competing financial interests or personal relationships that could have appeared to influence the work reported in this paper.

Availability of data and material

The data sets reported in this study are available from the corresponding author.

References

[1] Gauglitz, P.A., Friedmann, F., Kam, S.I., and Rossen, W.R. 2002, April. Foam generation in porous media. In SPE/DOE Improved Oil Recovery Symposium. OnePetro. https://doi.org/10.2118/75177-MS.

[2] W.R. Rossen, Foams in enhanced oil recovery in Foams: Theory, Measurements, and Application, ed, Prud'homme, Robert K. 57 (1996) 413–464.

[3] D.K. Kennedy, F.W. Kitziger, B.E. Hall, Case study on the effectiveness of nitrogen foams and water zone diverting agents in multistage matrix acid treatments, SPE Prod. Eng. 7 (02) (1992) 203–211, https://doi.org/10.2118/20621-PA.

[4] Hirasaki, G.J., Miller, C.A., Szafranski, R., Lawson, J.B., and Akiya, N. 1997. Surfactant/foam process for aquifer remediation. In International symposium on oilfield chemistry. SPE 37257-MS. https://doi.org/10.2118/37257-MS.

[5] A.R. Kovscek, C.J. Radke, Fundamentals of Foam Transport in Porous Media, in: L. L. Schramm (Ed.), Foams in the Petroleum Industry, 242, Amer. Chem. Soc., Washington, D.C., 1994, pp. 115–163.

[6] G.C. Bernard, L.W. Holm, C.P. Harvey, Use of surfactant to reduce CO2 mobility in oil displacement, Soc. Pet. Eng. J. 20 (04) (1980) 281–292, https://doi.org/10.2118/8370-PA.

[7] Bond, D.C. and Holbrook, O.C. 1958. U.S. Patent No. 2,866,507. Washington, DC: U.S. Patent and Trademark Office.

[8] A.N. Fried, The Foam-drive Process for Increasing the Recovery of Oil, US Department of the Interior, Bureau of Mines,, 1961.

[9] T.W. Patzek, Field applications of steam foam for mobility improvement and profile control, SPE Reserv. Eng. 11 (02) (1996) 79–86, https://doi.org/10.2118/29612-PA.

[10] W.R. Rossen, Foam in Porous Media. In Foams and Emulsions, Springer,, Dordrecht, 1999, pp. 335–348.

[11] J.M. Alvarez, H.J. Rivas, W.R. Rossen, Unified model for steady-state foam behavior at high and low foam qualities, SPE Journal 6 (03) (2001) 325–333, https://doi.org/10.2118/74141-PA.

[12] Cheng, L., Reme, A.B., Shan, D., Coombe, D.A., and Rossen, W.R. 2000, April. Simulating foam processes at high and low foam qualities. In SPE/DOE improved oil recovery symposium. OnePetro. https://doi.org/10.2118/59287-MS.

[13] Osterloh, W.T. and Jante, M.J. 1992, April. Effects of gas and liquid velocity on steady-state foam flow at high temperature. In SPE/DOE Enhanced Oil Recovery Symposium. OnePetro. https://doi.org/10.2118/24179-MS.

[14] Farajzadeh, R., Wassing, B., and Boerrigter, P. 2010, September. Foam assisted gas oil gravity drainage in naturally-fractured reservoirs. In SPE Annual Technical Conference and Exhibition. https://doi.org/10.2118/134203-MS.

[15] Å. Haugen, N. Mani, S. Svenningsen, B. Brattekås, A. Graue, G. Ersland, M.A. Fernø, Miscible and immiscible foam injection for mobility control and EOR in fractured oil-wet carbonate rocks, Transp. Porous Media 104 (1) (2014) 109–131, https://doi.org/10.1007/s11242-014-0323-6.

[16] A.R. Kovscek, D.C. Tretheway, P. Persoff, C.J. Radke, Foam flow through a transparent rough-walled rock fracture, J. Pet. Sci. Eng. 13 (2) (1995) 75–86, https://doi.org/10.1016/0920-4105(95)00005-3.

[17] Friedmann, F., Hughes, T.L., Smith, M.E., Hild, G.P., Wilson, A., and Davies, S.N. 1997, October. Development and testing of a new foam-gel technology to improve conformance of the Rangely CO2 flood. In SPE Annual Technical Conference and Exhibition. OnePetro. https://doi.org/10.2118/38837-MS.

[18] Ocampo-Florez, A., Restrepo, A., Rendon, N., Coronado, J., Correa, J.A., Ramirez, D.A., Torres, M., Sanabria, R., Lopera, S.H. 2014, December. Foams prove effectiveness for gas injection conformance and sweep efficiency improvement in a low porosity fractured reservoir–field pilots. In International Petroleum Technology Conference. OnePetro. https://doi.org/10.2523/IPTC-17950-MS.

[19] Katiyar, A., Patil, P.D., Rohilla, N., Rozowski, P., Evans, J., Bozeman, T., and Nguyen, Q. 2019, October. Industry-first hydrocarbon-foam EOR pilot in an unconventional reservoir: design, implementation, and performance analysis. In Unconventional Resources Technology Conference, Denver, Colorado, 22–24 July 2019 (pp. 233–255). Unconventional Resources Technology Conference (URTeC); Society of Exploration Geophysicists. ⟨https://doi.org/10.15530/urtec-2019–103⟩.

[20] Ocampo, A., Restrepo, A., Clavijo, J., and Mejía, J.M. 2020, August. Successful Foams EOR Field Pilot in a Naturally Fractured Reservoir by the Injection of the Foaming Agent Dispersed in the Gas Stream. In SPE Improved Oil Recovery Conference. Society of Petroleum Engineers. https://doi.org/10.2118/200377-MS.

[21] L.W. Lake, R.T. Johns, W.R. Rossen, G.A. Pope, Fundamentals of Enhanced Oil Recovery, Society of Petroleum Engineers,, Richardson, TX, 2014.

[22] J. Gong, S. Vincent-Bonnieu, R.Z. Kamarul Bahrim, C.A. Che Mamat, R.D. Tewari, M.I. Mahamad Amir, W.R. Rossen, Injectivity of multiple slugs in surfactant alternating gas foam EOR: a CT scan study, SPE Journal 25 (2020) 895–906, https://doi.org/10.2118/199888-PA.

[23] Tang, J., Vincent-Bonnieu, S., and Rossen, W.R. 2019, September. CT Coreflood Study of Transient Foam Flow with Oil. In SPE Annual Technical Conference and Exhibition. Society of Petroleum Engineers. https://doi.org/10.2118/196202-MS.

[24] J. Gauteplass, K. Chaudhary, A.R. Kovscek, M.A. Fernø, Pore-level foam generation and flow for mobility control in fractured systems, Colloids Surf. A: Physicochem. Eng. Asp. 468 (2015) 184–192, https://doi.org/10.1016/j.colsurfa.2014.12.043.

[25] B.I. AlQuaimi, W.R. Rossen, Foam generation and rheology in a variety of model fractures, Energy Fuels 33 (1) (2018) 68–80, https://doi.org/10.1021/acs.energyfuels.8b02178.

[26] S.A. Jones, N. Getrouw, S. Vincent-Bonnieu, Foam flow in a model porous medium: II. The effect of trapped gas, Soft Matter 14 (18) (2018) 3497–3503, https://doi.org/10.1039/C7SM02458D.

[27] P.A. Witherspoon, J.S. Wang, K. Iwai, J.E. Gale, Validity of cubic law for fluid flow in a deformable rock fracture, Water Resour. Res. 16 (6) (1980) 1016–1024, https://doi.org/10.1029/WR016i006p01016.

[28] K. Li, K.H.A.A. Wolf, W.R. Rossen, Effects of gas trapping on foam mobility in a model fracture, Transp. Porous Media 138 (2021) 185–200, https://doi.org/10.1007/s11242-021-01598-y.

[29] V. Bergeron, C.J. Radke, Equilibrium measurements of oscillatory disjoining pressures in aqueous foam films, Langmuir 8 (12) (1992) 3020–3026, https://doi.org/10.1021/la00048a028.

[30] G.J. Hirasaki, Wettability: fundamentals and surface forces, SPE Form. Eval. 6 (02) (1991) 217–226, https://doi.org/10.2118/17367-PA.